RSC Advances

PAPER

View Article Online
View Journal | View Issue

Cite this: *RSC Adv.*, 2016, **6**, 52509

A facile method for transparent carbon nanosheets heater based on polyimide†

Hamid Souri,‡[a] Seong Jun Yu,‡[b] Hyeonuk Yeo,[a] Munju Goh,[a] Jun-Yeon Hwang,[a] Seung Min Kim,[a] Bon-Cheol Ku,[a] Young Gyu Jeong*[b] and Nam-Ho You*[a]

Received 22nd March 2016
Accepted 20th May 2016

DOI: 10.1039/c6ra07457j

www.rsc.org/advances

In this work, a novel film heater in nanometer-scale thickness based on catalyst-free and transfer-free carbon nanosheets (CNSs) with properties similar to graphene is fabricated. Here, poly(amic acid) (PAA), which is composed of several aromatic hydrocarbon rings, is used as the carbon precursor of CNS films. Altering the polymer concentration easily controls the morphological, optical, and electrical properties of the CNS films obtained by carbonization of PAA thin films. The CNS films with different thicknesses of 7.53–28.40 nm are simply prepared through spin-coating on a quartz substrate and post heat-treatment. Finally, their direct use as transparent film heaters is deeply investigated by considering electrical conductivity, temperature response rapidity, achievable maximum temperature, and electric power efficiency. For instance, an electrically conductive and optically transparent CNS film with 28.40 nm thickness exhibits excellent electric heating performance achieving well-defined steady-state maximum temperatures of 24–333 °C at low input electric power per unit film area of 0.027–1.005 W cm^{-2} in a relatively short time of ~100 s.

Introduction

Thick-film heaters have been vastly used in recent times due to their interesting properties. In particular, transparent and flexible film heaters have attracted considerable attention from researchers for a wide range of applications such as vehicle window defrosters, heat retaining windows, avionics, displays, and medical devices.[1–3] The traditional alloy-based film heaters with brittle and opaque moieties have been shown to be ineffective in mass production and practical use due to their complicated fabrication process, heavy weight, and low heating efficiency.[4–6] In addition, while indium tin oxide (ITO)-based transparent film heaters have also shown high transparency and electrical conductivity, the lack of indium resources and their fragility under external deformation have limited their use as film heaters.[7,8] Such other candidates as carbon nanotube (CNT)- and silver nanowire (AgNW)-based film heaters have been studied extensively and shown to be excellent choices to produce film heaters.[9–11] Yoon *et al.* investigated the electric heating performance of single-walled CNT (SWCNT) films, which were fabricated by a vacuum filtration method and transferred to glass or PET substrates.[12] A resulting SWCNT film with sheet resistance of 1190 Ω sq^{-1} and optical transparency of 91.3% exhibited better electric heating performance compared with exiting Ag films by consuming much less electric power to reach a target temperature. Jang *et al.* manufactured a transparent multi-walled CNT (MWCNT) film heater from a vertically-aligned MWCNT forest and transferring them on a PET film or glass substrate.[13] The single and double MWCNT sheet-based film heaters, which were characterized to have sheet resistances between 349 Ω sq^{-1} to 699 Ω sq^{-1} and transmittances range of 67–85%, showed rapid thermal responses and uniform temperature distribution when exposed to direct current. However, there are several limitations for the CNT film heaters in aspects of the environmental durability, surface structural damage, mass production, optical and electrical properties.[14,15]

In the recent time, graphene has attracted much of researchers' attention due to its superior electrical, mechanical, and chemical properties.[16–22] Moreover, graphene has shown outstanding optical transparency properties.[23–26] Considering these facts, the use of graphene as a nano-sized filler in a number of different interesting applications has been reported.[27–29] In order to synthesize graphene, researchers have mainly used one of the following methods; (1) micro-mechanical exfoliation of graphite, (2) chemical vapor deposition (CVD), and (3) chemical reduction of graphene oxide

[a]*Carbon Composite Materials Research Center, Institute of Advanced Composites Materials, Korea Institute of Science and Technology, Eunha-ri San 101, Bondong-eup, Wanju-gun, Jeollabuk-do, 565-905, Republic of Korea. E-mail: polymer@kist.re.kr*

[b]*Department of Advanced Organic Materials and Textile System Engineering, Chungnam National University, Daejeon 34234, Korea. E-mail: ygjeong@cnu.ac.kr*

† Electronic supplementary information (ESI) available: Additional characterization of CNSs including Raman and XPS spectra are provided. In addition, time-dependent temperature changes of the CNS films under various applied voltages are available. See DOI: 10.1039/c6ra07457j

‡ These authors contributed equally.

(GO).[30–33] Each of these routes has exhibited some advantages and disadvantages. For instance, while the micro-mechanical exfoliation results in high quality graphene; it has the disadvantage of yielding low amount of carbon compared to the other methods.[34–36] Although high quality and large sized graphene can be produced by CVD method, the process requires careful control to obtain uniform growth of graphene, making this process complicated.[37,38] In addition, the complexity of transfer process can be referred to as one of the other disadvantages of this method.[39,40] When GO is used to synthesize, large amount of graphene can be obtained with low cost. However, the quality of the resulting graphene would be lower compared to other methods due to the extensive modification of graphene.[41–43] As a result, finding new routes to achieve development of high quality and transfer-free graphene have been desired and researched, but there are some drawbacks such as availability only under certain extreme production conditions, low productivity, and complicated procedure.

Recently, novel methods to acquire carbon nanosheets (CNSs) as an alternative of graphene have been explored. These show analogous properties to graphene from solid carbon sources, especially organic polymers.[44–46] In this regard, some specific polymers such as poly(methyl methacrylate) (PMMA), polystyrene (PS), polyacetylene (PAc), and polyacrylonitrile (PAN) have been widely used to prepare CNSs due to their good film-forming properties and high carbonization yield.[47–50] In particular, the carbonization process of these polymers has been mainly studied for production of porous carbons in addition to CNSs. While polyimide (PI) or polymer of imide monomers is being used as a carbon precursor,[51] there has been only a few research for fabrication of thin carbon sheets using PIs. It has the potential to use PIs as a CNS precursor with a facile procedure with high carbonization yield and highly oriented intermolecular structure. In particular, carbonization method of polyimide has been a good candidate of transfer-free CNSs synthesis for mass production. The synthetic procedure of CNSs from the PIs would not be necessary to attach its film to any substrates because its self-stand films are very easy to produce. In addition, because PIs have highly oriented molecular structure originated from those rigid back-bone structure, strong intermolecular interaction, and charge transfer complexes between electron donor and electron acceptor moieties,[52–54] CNS devoid of any fracture can be obtained, even though pyrolitic process was involved.[55,56]

In this study, a catalyst-free and transfer-free process using aromatic PI precursors was used. We synthesized poly(amic acid) (PAA) precursor from pyromellitic dianhydride (PMDA) and 3,3′-dihydroxybenzidine (DHB). The chemical structure of the PAA has ortho-substituted hydroxyl groups of DHB units, which can promote thermal rearrangement from PI to polybenzoxazole (PBO).[57,58] Afterwards, thin CNS films with excellent electrical conductivity and chemical stability were easily prepared by spin-coating of PAA solution onto quartz substrates, followed by the carbonization process which can take place at up to 1100 °C. In carbonization process, the PAA films would be converted to CNSs *via* each stage of PIs and PBOs. The high thermal stability and strong intermolecular interaction of PBO was able to improve both carbon yield and retention of the film during CNS production.[59,60] The CNS thin films in nanometer-scale thickness were then characterized to fully understand their optical, thermal, and electrical properties. The electric heating performance of the CNS films with high optical transparency exhibited excellent electric heating performance in terms of temperature responsiveness, maximum temperatures and electric power efficiency at applied voltages of 10–100 V. The results indicate that the CNSs derived from PAA solution can be an excellent candidate to develop film heaters which can be used in a wide range of applications.

Experimental section

Materials

3,3′-Dihydroxybenzidine (DHB), pyromellitic dianhydride (PMDA), and *N*-methyl-2-pyrrolidone (NMP, 99.5%) were as a proprietary product of Wakayama Seika Kogyo (Japan), Tokyo Chemical Industry Co., Ltd. (Japan), and Sigma-Aldrich, respectively.

Synthesis of poly(amic acid) (PAA)

To synthesize PAA as a carbon precursor, 3,3′-dihydroxybenzidine (DHB, 0.99 g) was poured into *N*-methyl-2-pyrrolidone (NMP, 28.6 g). The solution was then stirred at room temperature for 2 hours. Subsequently, pyromellitic dianhydride (PMDA, 1.00 g) was introduced to the solution, and the mixture was stirred for 24 hours at room temperature. The resultant solution was then diluted with NMP to obtain a different concentration for polymer solution (see ESI, Scheme S1†).

Synthesis of CNS films

The polymer solutions ranging from 0.75 to 2.0 wt% were prepared. Prior to the spin-coating process, quartz substrates were cleaned by ethanol and isopropyl alcohol with the aid of a sonication bath for 40 minutes and dried in an oven. Substrates were then treated with UV ozone for 20 minutes. The spin-coating process was used to coat PAA films on the quartz substrates. Subsequently, PAA films were directly carbonized up to 1100 °C with an increase of 10 °C min^{-1} in the presence of the H_2/Ar mixture (ESI, Scheme S2†).

Characterization

The thickness and surface roughness of the obtained CNS thin films were characterized by atomic force microscopy (AFM, Park NX10, Park systems, Korea). To verify the degree of the structure development of CNS films, Raman spectroscopy (Horiba) with a 514.5 nm laser beam was employed. The sheet resistance of the CNS films was measured by a four-point probe (FPP Portable, Dasol Eng.), and their transmittance was analyzed by ultraviolet-visible spectroscopy (UV-Vis, V-570, Jasco). For further characterization, X-ray photoelectron spectroscopy (XPS, PHI 5000 Versa Probe, Ulvac-PHI) was used to identify the components of the CNSs. Moreover, to study the surficial morphology and structure properties of the CNS films, transmittance electron microscopy (TEM, Tecnai G2 F20, FEI) and

scanning electron microscopy (Nova NanoSEM, FEI, USA) were utilized. The electric heating performance of the CNS films was characterized with the aid of an infrared camera (SE/A325, FLIR Systems) and a source meter instrument (2400, Keithley Instruments Inc.). For the electric heating experiments, the silver electrodes were applied to the CNS films, and their distance was set at 10.0 mm.

Results and discussion

Characterization of CNSs

Prior to fabrication of PAA films, a PAA was synthesized from 3,3′-dihydroxybenzidine (DHB) and pyromellitic dianhydride (PMDA) in *N*-methyl-2-pyrrolidone (NMP) solvent (Scheme S1†). In particular, biphenylic hydroxyl groups of DHB moiety have been known to promote the growth of polybenzoxazole (PBO) structure during its pyrolysis.[61] For that reason, the pyrolysis process of the PAA was tracked by TGA studies under N_2 atmosphere (Fig. 1), which resulted in three steps weight loss and 45 wt% of total weight loss at 800 °C. The first weight loss started at 200 °C, which corresponds to conversion of the PAA to the PI structure mediated by a cyclodehydration process. In addition, the rearrangement of the PI to the PBO structure was observed in the second stage which started at 400 °C by cyclo-decarboxylation. Over 600 °C, the weight decrease by carbonization was shown, which was influenced by polymer pyrolysis and rearrangement.[75]

The NMP solutions containing the PAA of range from 0.75 to 2.0 wt% were prepared and casted by using spin coater on quartz substrates. The obtained PAA films were directly carbonized up to 1100 °C with a rate of 10 °C min^{-1} in H_2/Ar atmosphere (Scheme S2†). To measure the thickness and surface roughness of the CNS films as a function of the PAA concentration, atomic force microscopy (AFM) was employed, respectively. It was observed that the thickness of CNS films approximately linearly increased as the polymer concentration increased (Fig. 2).

The thickness values of CNS films derived from 0.75–2.0 wt% PAA solutions were ranged from 7 to 28 nm. On the other hand, the surface roughness values in the area of 5 × 5 μm^2 of CNS

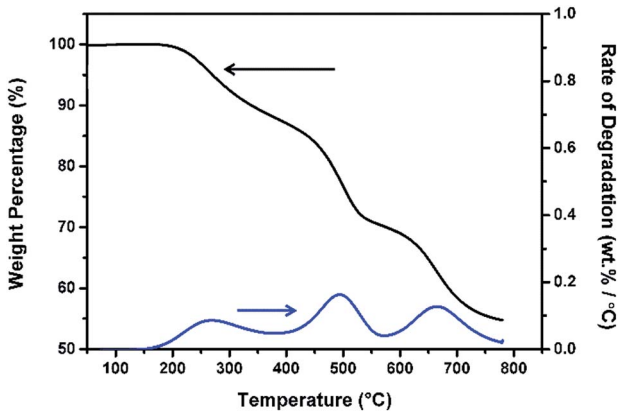

Fig. 1 TGA curve of PAA precursor.

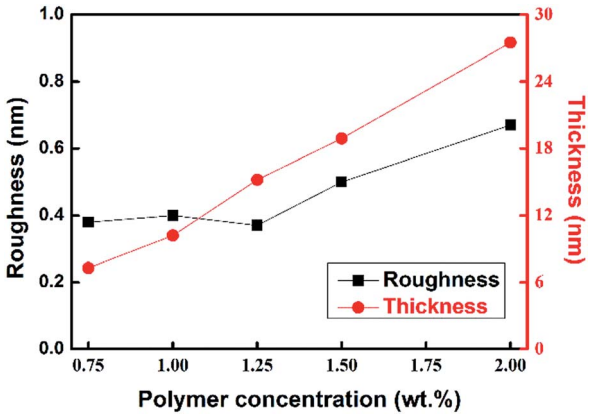

Fig. 2 Thickness and surface roughness of CNS films with regard to polymer concentration.

films converted from 0.75–1.25 wt% PAA solutions were approximately 0.4 nm. However, the surface roughness values of CNS films derived from 1.5 and 2.0 wt% PAA solutions were increased to 0.5 and 0.67 nm, respectively. The low level of surface roughness values represented a relatively flat surface, in which the occurrence of leakage current and shorts would be decreased.[62]

To understand the structural composition of the CNS films, X-ray photoelectron spectroscopy (XPS) was conducted. For all of the CNS film samples, carbon and oxygen atoms were the constituents of the CNS films after carbonization of the spin-coated PAA, as listed in Table 1.

As shown, the samples made of more than 1.25 wt% of PAA as carbon precursor consisted of more than 90% of carbon atoms, while the atomic percentage of oxygen for these samples was too low, indicating that the atoms in the PAA polymer chain were mostly removed because of the generated heat by the carbonization process. The C1s and O1s spectra of the CNS films converted from 1.0 wt% PAA solution are exhibited (Fig. 3). The C1s spectra for all of the samples showed a primary peak and two weak peaks corresponding to the binding energy values of 284.8, 286, and 288.5 eV related to C–C (sp^2 carbon), C–O, and O–C=O bonds, respectively.[63–66] The O1s spectra for various types of samples showed two peaks at approximately 530.9 and 532.5 eV, which can be attributed to C=O and C–O, respectively.[66] The C1s and O1s spectra related to the other polymer concentrations can be found in the ESI (Fig. S2†).

Table 1 Atomic concentration for the CNS films

CNS film thickness [nm]	Atomic composition (%)	
	C	O
7.53	75.33	24.67
10.20	78.94	21.06
15.21	90.00	10.00
17.32	94.54	5.46
28.40	96.46	3.54

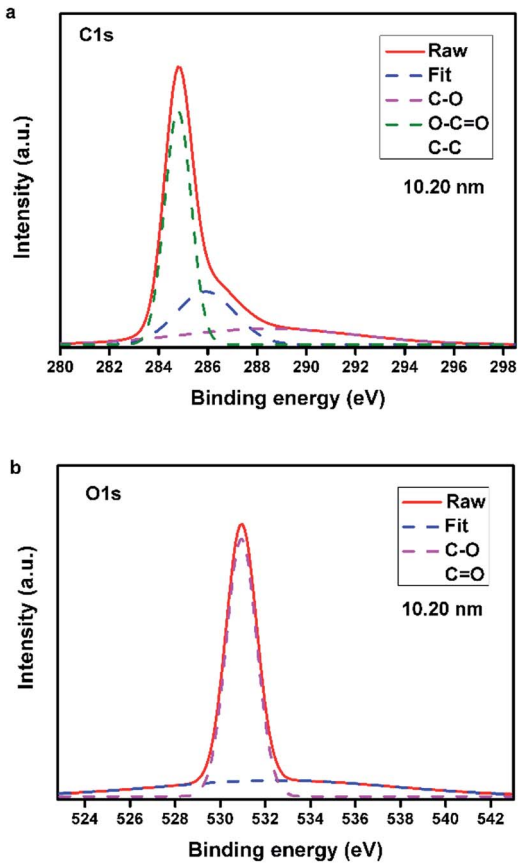

Fig. 3 (a) The deconvoluted XPS C1s, and (b) O1s spectra of the CNS film with thickness of 10.20 nm.

The Raman spectra of CNS film sample converted from 1.0 wt% PAA solution were carried out (Fig. 4). The D-band related to the disordered and defective structure of CNS films and G-band corresponding to the ordered carbon structure with sp^2 on CNS films were detected at about 1355–1360 cm^{-1} and 1585–1590 cm^{-1}, respectively. Two different points of each sample were selected to perform the Raman spectroscopy. Moreover, the I(G)/I(D) ratio was calculated for each spectrum. All of the samples showed the ratio to be greater than one, confirming the fact that a low number of defects were generated after carbonization within the CNSs structures. For instance, the CNS film converted from 1.0 wt% PAA solution showed I(G)/I(D) ratios to be 1.009 and 1.005 for two different points. In addition, all of the samples presented a negligible 2D band at about 2670–2675 cm^{-1} and a D + G band at about 2920–2925 cm^{-1}, indicating the multilayer structure of CNSs.[67] In addition, the Raman spectra for other CNS films synthesized by different PAA concentrations can be found in the ESI (Fig. S3†).

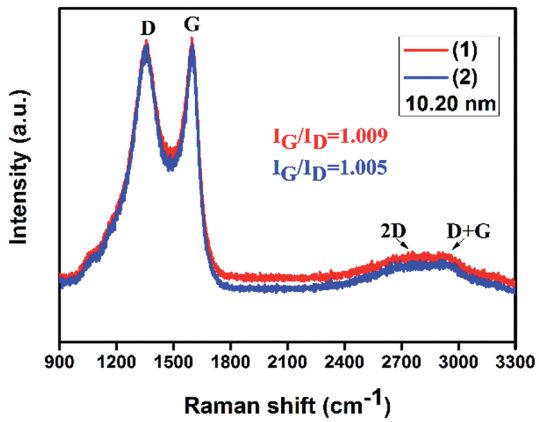

Fig. 4 Two representative Raman spectra of the CNS film with thickness of 10.20 nm.

The CNS films were characterized by high-resolution transmittance electron microscopy (HR-TEM) to check their graphitic structure (Fig. 5). The graphitic structure of the CNS films varies with regard to the PAA solution concentration, although they were carbonized under the same temperature condition. Son *et al.* reported this phenomenon as well.[63,64] This phenomenon can be explained as follows: at low polymer concentration (0.75 wt%), the resultant CNS films showed an amorphous structure (Fig. 5). In the case of using 1.25 wt% PAA solution, the CNS films exhibited curvy and short layers of graphene. As the polymer concentration increased to 1.5 and 2.0 wt%, the densely packed CNSs were clearly observed. These results confirmed the fact that the positioning and orientation of the CNSs could highly depend on the interaction between the chains in the precursor polymer and the spin-coated surface of the quartz substrate. After spin-coating process, precursor polymer chains can be randomly located on the substrate.

During carbonization process, the polymer chains can be excited by thermal energy and relocated. In the case of using low polymer concentration, the chains within polymer can firmly interact with the spin-coated surface of the substrate so that there would be lack of opportunity for the chains to freely relocate. On the contrary, the use of higher concentration of

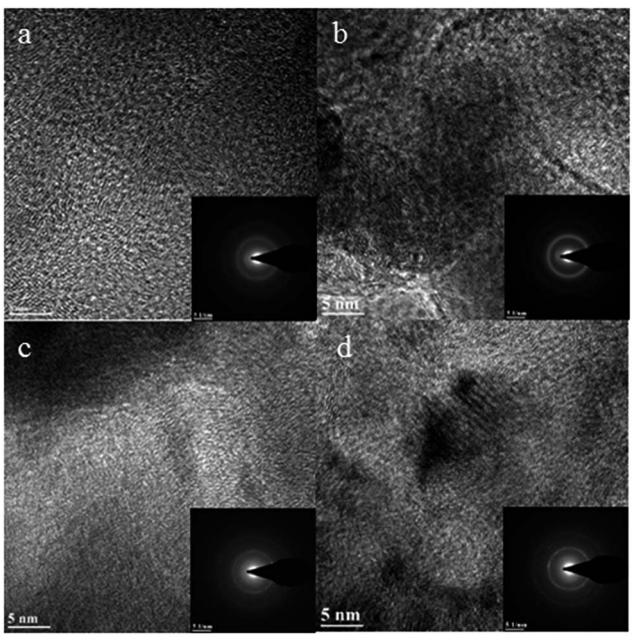

Fig. 5 HR-TEM images of CNS films with different thicknesses: (a) 7.53; (b) 10.20; (c) 17.32; (d) 28.40 nm.

polymer, which results in a thicker layer of spin-coated precursor polymer, can provide the chance for other polymer chains to easily move and form randomly compacted CNSs layers, while some portion of the polymer chains are connected to the spin-coated surface of the substrate. Consequently, the intermolecular condensation can be improved and the networks can be formed in relatively lower temperatures.[68,69]

To understand the structure of CNS films better, their selected area electron diffraction (SAED) patterns were captured (Fig. 5). The SAED patterns corresponded to the low polymer concentration and evidently presented a typical pattern of graphite or multi-layered graphite sheets without any special pattern on SAED image, which represents a comparatively lower crystallinity structure (Fig. 5(a) inset). On the other hand, as the polymer concentration increased, the SAED patterns clearly exhibited the diffused rings in which these patterns were found to be similar as graphene. The clear spots attributed to the reflections in the rings of CNS films confirmed a high crystallinity in CNSs structures converted from high contents of polymer without the presence of any undesired structure.[70]

In addition to TEM analysis, scanning electron microscopy (SEM) images were used to study the surface morphology of the CNS films (Fig. 6). The CNS films converted from low polymer concentrations show comparatively higher impurities on the surface of CNS films, while the CNS film derived from 1.5 wt% PAA solution exhibits a low level of impurities with the smooth surface. This phenomenon might be due to the very low level of film thickness of CNS films converted from a low amount of polymers.

Optical and electrical properties of carbon nanosheets

A four-point probe method was utilized to measure the sheet resistance (R_{sheet}) of the CNS films. As the polymer concentration increased, the sheet resistance values decreased. These values were ranged from 14.7 to 1.6 kΩ sq^{-1} for 7.53–28.40 nm thick CNS films (Fig. 7). The electrical conductivity values for various CNS films were calculated using the following equation:

$$\sigma = \frac{1}{(R_{sheet} \times t)} \quad (1)$$

where, σ denotes the electrical conductivity, t represents the film thickness, and R_{sheet} is the value of sheet resistance obtained by a four-point probe method. The obtained conductivity values were ranged from 94 to 218 S cm^{-1}, in which they were comparable to those reported in the literature, indicating the potential application of CNS films as transparent thin films.[62,71] The optical transmittance of the CNS films decreased as the film thickness or polymer concentration increased (Fig. 7).

The optical transmittance values of the CNS films at 550 nm of wavelength are demonstrated as a function of the film thickness (Fig. 7). As shown in the figure, the transparency of CNS films on the quartz substrates was controlled by the concentration of the polymer resulting in different thicknesses. The transmittance values obtained for the CNS films in this study at the wavelength of 550 nm were approximately 89% at 7.53 nm, 88% at 10.20 nm, 77% at 15.21 nm, 67% at 17.32 nm, and 54% at 2.0 28.40 nm of film thicknesses, respectively. As can be seen, the word "KIST" could be easily detected under the sample with 15.21 nm thickness (Fig. 8). The minimum values of transmittance were recognized to be approximately 270 nm for all of the samples. This confirms the fact that the CNS films own graphitic structures.[71]

Electro-thermal properties

The electric heating behavior of the CNS thin films with different thicknesses was analyzed by monitoring temperature changes under constant voltages of 10–100 V. Fig. 9 represents typical time-dependent temperature changes of a CNS film with 28.40 nm thickness under a variety of applied voltages. The temperatures of the CNS film increased as soon as a certain applied voltage above 10 V was applied, reached steady-state maximum values within ~100 s, and decreased quickly to an ambient temperature when the applied voltage was off. This electric heating behavior was also identical for other CNS films with different thicknesses, as can be seen in the ESI (Fig. S4†).

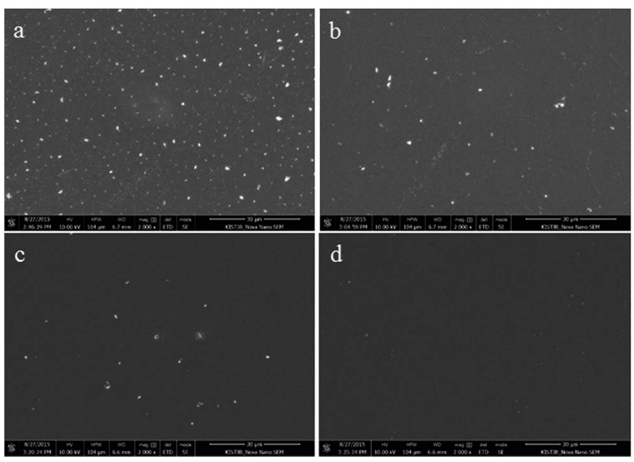

Fig. 6 SEM images of CNS films with different thicknesses: (a) 7.53; (b) 10.20; (c) 15.21; (d) 17.32 nm.

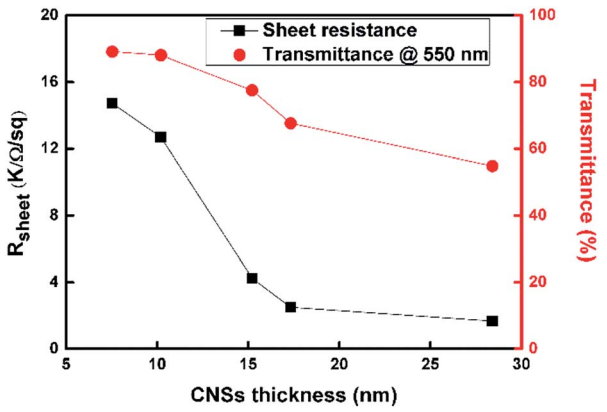

Fig. 7 Sheet resistance and optical transmittance values at 550 nm of CNS films *versus* CNSs film thickness.

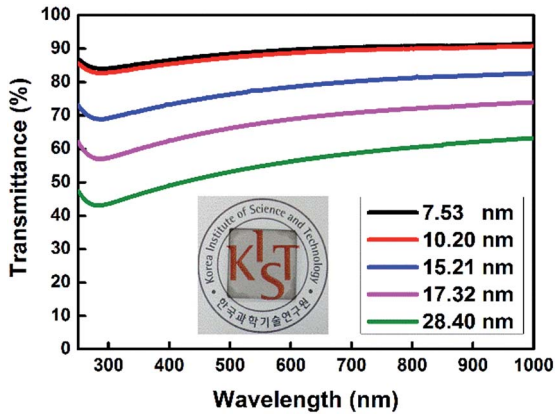

Fig. 8 Optical transmittance of CNS films with different thicknesses of 7.53–28.40 nm. The inset exhibits a photographic image of a CNS film with 15.21 nm thickness.

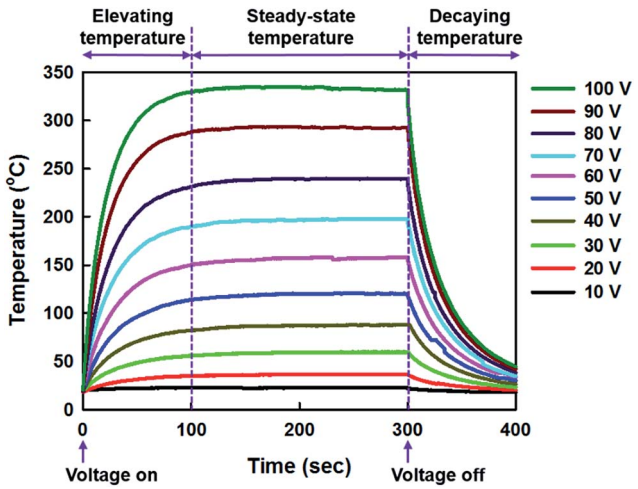

Fig. 9 Time-dependent temperature changes of a CNS film with 17.32 nm thickness at a variety of applied voltages of 10–100 V.

To investigate the electric heating performance of the CNS films in detail, characteristic parameters related to temperature responsiveness and energy efficiency at given applied voltages were obtained from the experimental time-dependent temperature curves in Fig. 9, which could be separated into elevating temperature (heating), steady-state temperature (equilibrium), and decaying temperature (cooling) stages. The first stage of elevating temperature with time can be expressed as the following equation:[72–74]

$$\frac{T_t - T_i}{T_{max} - T_i} = 1 - \exp\left(-\frac{t}{\tau_g}\right) \quad (2)$$

where T_i is the initial ambient temperature, T_{max} is the steady-state maximum temperature, and T_t is an arbitrary temperature at time τ_g is the characteristic growth time constant, which can be evaluated as an adjustable parameter to fit the first part of the time–temperature curves (Table 2). At the second stage of the steady-state maximum temperatures at applied voltages, the heat gain by inputting electric power is equal to the heat loss by radiation and convection based on the conservation law of energy. Accordingly, the heat transferred by radiation and convection, h_{r+c}, can be evaluated by[72–74]

$$h_{r+c} = \frac{P_{in}}{T_{max} - T_i} = \frac{IV}{T_{max} - T_i} \quad (3)$$

where I is the steady-state current conducted through a film heater at an applied voltage V. The calculated h_{r+c} values for all the CNS films at different applied voltages were summarized (Table 2). At the third stage, the temperature decay with time can be described by the following empirical formula:

$$\frac{T_t - T_f}{T_{max} - T_f} = \exp\left(-\frac{t}{\tau_d}\right) \quad (4)$$

where T_f is the final ambient temperature and τ_d is the characteristic decay time constant. The τ_d values of the CNS films were then calculated by fitting experimental time-dependent temperature decay data (Table 2). All of the characteristic parameters of τ_g, τ_d, and h_{r+c} associated with the electric heating behavior have decreasing trends with the film thickness. The lower τ_g and τ_d values for the thicker CNS films are believed to be caused by the higher thermal and electrical conductivity, which demonstrates the higher temperature response rapidity at given applied voltages. In addition, the lowered h_{r+c} values for the thicker CNS films indicate that the CNS films with higher electrical conductivity have higher electric energy efficiency, because they need relatively lower electrical energy to maintain steady-state maximum temperatures at given applied voltages.

On the other hand, the steady-state maximum temperatures (T_{max}) were found to increase with the increment of the applied voltage as well as the film thickness (Fig. 11). At a fixed applied voltage, the CNS films with higher thickness could reach higher T_{max} values due to their higher electrical conductivity, and for a given CNS film, the T_{max} values also increased quadratically

Table 2 Characteristic parameters of electric heating performance of CNS films with different thicknesses

CNS film thickness [nm]	Voltage [V]	τ_g [s]	τ_d [s]	h_{r+c} [mW °C^{-1}]
7.53	10–100	31.5 ± 3.3	28.2 ± 2.7	15.2 ± 1.4
10.20	10–100	27.2 ± 2.1	18.9 ± 1.2	8.5 ± 1.4
15.21	10–100	20.7 ± 2.2	18.6 ± 0.3	7.5 ± 1.8
17.32	10–100	19.2 ± 1.4	18.0 ± 0.6	7.5 ± 2.0
28.40	10–90	17.6 ± 0.6	17.9 ± 0.4	6.3 ± 2.7

with the increment of the applied voltage. For instance, the 28.40 nm thick CNS film attained T_{max} of ~76 and ~315 °C at applied voltages of 30 and 80 V, respectively, which were far higher than those (~25 °C at 30 V and ~74 °C at 80 V) of the 7.53 nm thick CNS film. The quadratic increments of T_{max} with the applied voltage in Fig. 10 are consistent with the quadratic change of input electric power with applied voltage, which is expressed as $P_{in} = IV = V^2/R$, where P_{in} is the input electric power and R the electrical resistance. It means that the input electric power applied to the CNS films was effectively converted to thermal energy as heat, which is dissipated to the surrounding environment. As the result, the T_{max} of all the CNS films increased linearly with the P_{in} (Fig. 10). Accordingly, a well-defined maximum temperature for a CNS film heater can be efficiently attained by controlling input electric power per unit film area, based on the relation of $T_{max} = 326.4P_{in} + 29.5$.

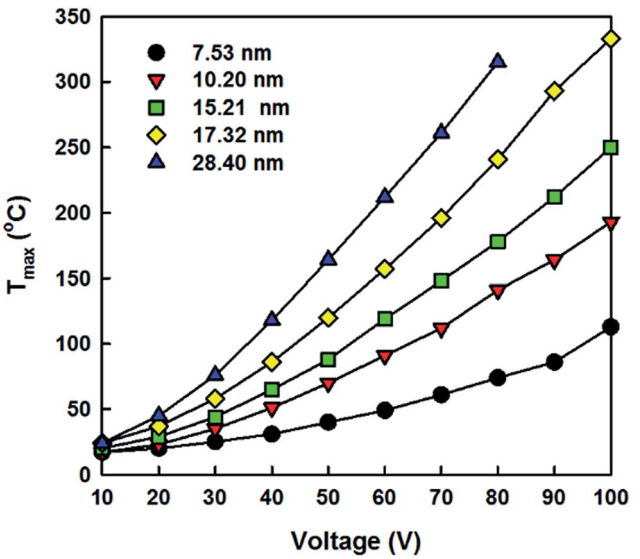

Fig. 10 Steady-state maximum temperatures (T_{max}) of CNS films with different thicknesses as a function of the applied voltage.

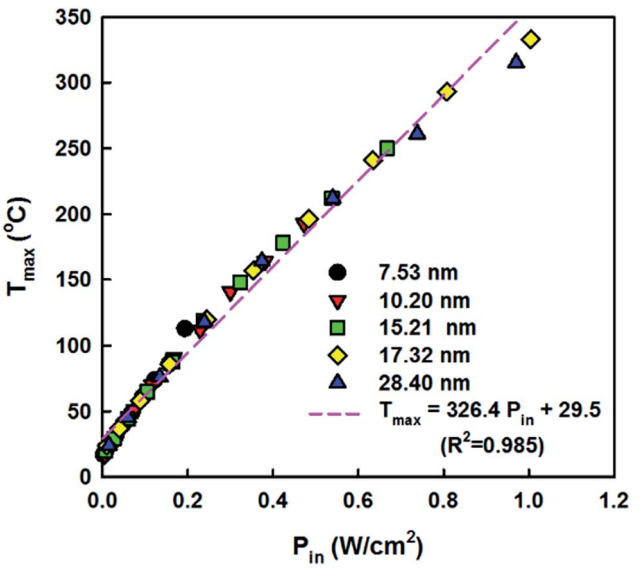

Fig. 11 Steady-state maximum temperatures (T_{max}) of CNS films with different thicknesses as a function of the input electric power (P_{in}).

Conclusions

In this study, electrically conductive and optically transparent CNS films with 7.53–28.40 nm thickness were manufactured by an efficient catalyst-free and transfer-free process of spin-coating PAA thin films on a quartz substrate and following carbonization. The structures, optical and electrical properties of the CNS films were characterized as a function of the film thickness. XPS, TEM, SAED, Raman, and SEM results supported that high crystalline carbon nanosheets were developed in the CNS films without the presence of any undesired structure. The electrical conductivity of the CNS films increased from 94 to 218 S cm^{-1} with the increase of the film thickness from 7.53 to 28.40 nm, although the optical transmittance at 550 nm decreased slightly from 89 to 54%. All of the CNS films with high electrical conductivity exhibited excellent temperature response rapidity as well as electric power efficiency in the applied voltage range of 10–100 V. In the case of 28.40 nm thick CNS film, a variety of steady-state maximum temperatures of 24–333 °C can be controlled at low input electric power per unit film area of 0.027–1.005 W cm^{-2} in a relatively short period time of ~100 s. It is thus reasonable to contend that the CNS film has great potential as high performance advanced transparent film heater in the application area including automobiles, smart windows, and medical devices for deicing, defrosting, and warming.

Acknowledgements

This work was supported by a grant from the Korea Institute of Science and Technology (KIST) institutional program (2Z04700), the Converging Research Center Program funded by the Ministry of Science, ICT & Future Planning Technology (2014M3C1A8054009), Basic Science Research Program through the National Research Foundation of Korea (NRF) funded by the Ministry of Science, ICT & Future Planning (2014R1A1A1002636), by a grant from the Ministry of Trade, Industry & Energy of Korea (2MR3560), and by the National Research Foundation of Korea (NRF) Grant funded by the Korean Government (MOE) (2013R1A1A2A10010080).

Notes and references

1 T. Kim, Y. W. Kim, H. S. Lee, H. Kim, W. S. Yang and K. S. Suh, *Adv. Funct. Mater.*, 2013, **23**, 1250–1255.
2 D. Sui, Y. Huang, L. Huang, J. Liang, Y. Ma and Y. Chen, *Small*, 2011, **7**, 3186–3192.
3 J. Kang, H. Kim, K. S. Kim, S.-K. Lee, S. Bae, J.-H. Ahn, Y.-J. Kim, J.-B. Choi and B. H. Hong, *Nano Lett.*, 2011, **11**, 5154–5158.
4 B. H. Liu, F.-Y. Liao and J.-H. Chen, *Thin Solid Films*, 2013, **537**, 263–268.

5 H. Sawai, T. Kanamori, I. Koiwa, S. Shibata, K. Nihei and T. Osaka, *J. Electrochem. Soc.*, 1990, **137**, 3653–3660.
6 H.-G. Cheong, J.-H. Kim, J.-H. Song, U. Jeong and J.-W. Park, *Thin Solid Films*, 2015, **589**, 633–641.
7 K. Im, K. Cho, J. Kim and S. Kim, *Thin Solid Films*, 2010, **518**, 3960–3963.
8 N. Kwon, K. Kim, J. Heo, I. Yi and I. Chung, *Nanotechnology*, 2014, **25**, 265702.
9 X. Zhang, X. Yan, J. Chen and J. Zhao, *Carbon*, 2014, **69**, 437–443.
10 S. Ji, W. He, K. Wang, Y. Ran and C. Ye, *Small*, 2014, **10**, 4951–4960.
11 D. Kim, L. Zhu, D.-J. Jeong, K. Chun, Y.-Y. Bang, S.-R. Kim, J.-H. Kim and S.-K. Oh, *Carbon*, 2013, **63**, 530–536.
12 Y.-H. Yoon, J.-W. Song, D. Kim, J. Kim, J.-K. Park, S.-K. Oh and C.-S. Han, *Adv. Mater.*, 2007, **19**, 4284–4287.
13 H.-S. Jang, S. K. Jeon and S. H. Nahm, *Carbon*, 2011, **49**, 111–116.
14 P. Liu, D. Zhou, Y. Wei, K. Jiang, J. Wang, L. Zhang, Q. Li and S. Fan, *ACS Nano*, 2015, **9**, 3753–3759.
15 P. Liu, L. Liu, K. Jiang and S. Fan, *Small*, 2011, **7**, 732–736.
16 F. Meng, W. Lu, Q. Li, J.-H. Byun, Y. Oh and T.-W. Chou, *Adv. Mater.*, 2015, **27**, 5113–5131.
17 R. Raccichini, A. Varzi, S. Passerini and B. Scrosati, *Nat. Mater.*, 2015, **14**, 271–279.
18 S. P. Surwade, S. N. Smirnov, I. V. Vlassiouk, R. R. Unocic, G. M. Veith, S. Dai and S. M. Mahurin, *Nat. Nanotechnol.*, 2015, **10**, 459–469.
19 H. Xia, C. Hong, B. Li, B. Zhao, Z. Lin, M. Zheng, S. V. Savilov and S. M. Aldoshin, *Adv. Funct. Mater.*, 2015, **25**, 627–635.
20 Y. Hou, Z. Wen, S. Cui, S. Ci, S. Mao and J. Chen, *Adv. Funct. Mater.*, 2015, **25**, 871.
21 S. Porada, P. Biesheuvel and V. Presser, *Adv. Funct. Mater.*, 2015, **25**, 179–181.
22 C. Wu, J. Maier and Y. Yu, *Adv. Funct. Mater.*, 2015, **25**, 3488–3496.
23 X. Wang, L. Zhi, N. Tsao, Ž. Tomović, J. Li and K. Müllen, *Angew. Chem.*, 2008, **120**, 3032–3034.
24 S. Bae, H. Kim, Y. Lee, X. Xu, J.-S. Park, Y. Zheng, J. Balakrishnan, T. Lei, H. R. Kim and Y. I. Song, *Nat. Nanotechnol.*, 2010, **5**, 574–578.
25 J. J. Bae, S. C. Lim, G. H. Han, Y. W. Jo, D. L. Doung, E. S. Kim, S. J. Chae, T. Q. Huy, N. Van Luan and Y. H. Lee, *Adv. Funct. Mater.*, 2012, **22**, 4819–4826.
26 G. T. Kim, S. J. Gim, S. M. Cho, N. Koratkar and I. K. Oh, *Adv. Mater.*, 2014, **26**, 5166–5172.
27 J. Liang, Y. Huang, L. Zhang, Y. Wang, Y. Ma, T. Guo and Y. Chen, *Adv. Funct. Mater.*, 2009, **19**, 2297–2302.
28 K. W. Putz, O. C. Compton, M. J. Palmeri, S. T. Nguyen and L. C. Brinson, *Adv. Funct. Mater.*, 2010, **20**, 3322–3329.
29 Y. T. Park, Y. Qian, C. Chan, T. Suh, M. G. Nejhad, C. W. Macosko and A. Stein, *Adv. Funct. Mater.*, 2015, **25**, 575–585.
30 S. Eigler, M. Enzelberger-Heim, S. Grimm, P. Hofmann, W. Kroener, A. Geworski, C. Dotzer, M. Röckert, J. Xiao and C. Papp, *Adv. Mater.*, 2013, **25**, 3583–3587.
31 J. A. Torres and R. B. Kaner, *Nat. Mater.*, 2014, **13**, 328–329.
32 D. Geng, H. Wang and G. Yu, *Adv. Mater.*, 2015, **27**, 2821–2837.
33 R. M. Jacobberger, B. Kiraly, M. Fortin-Deschenes, P. L. Levesque, K. M. McElhinny, G. J. Brady, R. R. Delgado, S. S. Roy, A. Mannix and M. G. Lagally, *Nat. Commun.*, 2015, **6**(8006), 1–8.
34 Y. Zhu, S. Murali, W. Cai, X. Li, J. W. Suk, J. R. Potts and R. S. Ruoff, *Adv. Mater.*, 2010, **22**, 3906–3924.
35 B. Jiang, C. Tian, L. Wang, Y. Xu, R. Wang, Y. Qiao, Y. Ma and H. Fu, *Chem. Commun.*, 2010, **46**, 4920–4929.
36 S. Park and R. S. Ruoff, *Nat. Nanotechnol.*, 2009, **4**, 217–224.
37 X. Li, W. Cai, J. An, S. Kim, J. Nah, D. Yang, R. Piner, A. Velamakanni, I. Jung and E. Tutuc, *Science*, 2009, **324**, 1312–1314.
38 L. Lin and Z. Liu, *Nat. Mater.*, 2016, **15**, 9–10.
39 Y. Zhu, S. Murali, W. Cai, X. Li, J. W. Suk, J. R. Potts and R. S. Ruoff, *Adv. Mater.*, 2010, **22**, 706–710.
40 X. Li, C. W. Magnuson, A. Venugopal, J. An, J. W. Suk, B. Han, M. Borysiak, W. Cai, A. Velamakanni and Y. Zhu, *Nano Lett.*, 2010, **10**, 4328–4334.
41 G. Eda, G. Fanchini and M. Chhowalla, *Nat. Nanotechnol.*, 2008, **3**, 270–274.
42 D. R. Dreyer, S. Park, C. W. Bielawski and R. S. Ruoff, *Chem. Soc. Rev.*, 2010, **39**, 228–240.
43 C. K. Chua and M. Pumera, *Chem. Soc. Rev.*, 2014, **43**, 291–312.
44 S. Stankovich, D. A. Dikin, R. D. Piner, K. A. Kohlhaas, A. Kleinhammes, Y. Jia, Y. Wu, S. T. Nguyen and R. S. Ruoff, *Carbon*, 2007, **45**, 1558–1565.
45 A. V. Murugan, T. Muraliganth and A. Manthiram, *Chem. Mater.*, 2009, **21**, 5004–5006.
46 H.-L. Guo, X.-F. Wang, Q.-Y. Qian, F.-B. Wang and X.-H. Xia, *ACS Nano*, 2009, **3**, 2653–2659.
47 H.-I. Joh, S. Lee, T.-W. Kim, S. Y. Hwang and J. R. Hahn, *Carbon*, 2013, **55**, 299–304.
48 S. Matsushita and K. Akagi, *J. Am. Chem. Soc.*, 2015, **137**, 9077–9087.
49 Z. Sun, Z. Yan, J. Yao, E. Beitler, Y. Zhu and J. M. Tour, *Nature*, 2010, **468**, 549–552.
50 S.-J. Byun, H. Lim, G.-Y. Shin, T.-H. Han, S. H. Oh, J.-H. Ahn, H. C. Choi and T.-W. Lee, *J. Phys. Chem. Lett.*, 2011, **2**, 493–497.
51 Z. Xu, X. Zhuang, C. Yang, J. Cao, Z. Yao, Y. Tang, J. Jiang, D. Wu and X. Feng, *Adv. Mater.*, 2016, **28**, 1981–1987.
52 M. Ghosh, *Polyimides: fundamentals and applications*, CRC Press, 1996.
53 K. Vanherck, G. Koeckelberghs and I. F. Vankelecom, *Prog. Polym. Sci.*, 2013, **38**, 874–896.
54 D.-J. Liaw, K.-L. Wang, Y.-C. Huang, K.-R. Lee, J.-Y. Lai and C.-S. Ha, *Prog. Polym. Sci.*, 2012, **37**, 907–974.
55 M. Inagaki, N. Ohta and Y. Hishiyama, *Carbon*, 2013, **61**, 1–21.
56 J. B. In, B. Hsia, J.-H. Yoo, S. Hyun, C. Carraro, R. Maboudian and C. P. Grigoropoulos, *Carbon*, 2015, **83**, 144–151.
57 K. Zhang, J. Liu and H. Ishida, *Macromolecules*, 2014, **47**, 8674–8681.
58 J. H. Chang, K. M. Park, S. M. Lee and J. B. Oh, *J. Polym. Sci., Part B: Polym. Phys.*, 2000, **38**, 2537–2545.

59 S. H. Han, N. Misdan, S. Kim, C. M. Doherty, A. J. Hill and Y. M. Lee, *Macromolecules*, 2010, **43**, 7657–7667.
60 M. B. Vázquez-Santos, A. Martínez-Alonso, J. M. Tascón, J.-N. Rouzaud, E. Geissler and K. Laszlo, *Carbon*, 2011, **49**, 2960–2970.
61 J. H. Chang, D. K. Park and K. J. Ihn, *J. Polym. Sci., Part B: Polym. Phys.*, 2001, **39**, 471–476.
62 L. De Arco Gomez, Y. Zhang, C. W. Schlenker, K. Ryu, M. E. Thompson and C. Zhou, *ACS Nano*, 2010, **4**, 2865–2873.
63 S. Y. Son, Y. J. Noh, C. S. Bok, S. Lee, B. G. Kim, S. I. Na and H. I. Joh, *Nanoscale*, 2014, **6**, 678–682.
64 S. W. Lee, C. Mattevi, M. Chhowalla and R. M. Sankaran, *J. Phys. Chem. Lett.*, 2012, **3**, 772–777.
65 A. Ganguly, S. Sharma, P. Papakonstantinou and J. Hamilton, *J. Phys. Chem. C*, 2011, **115**, 17009–17019.
66 M. H. Rummeli, A. Bachmatiuk, A. Scott, F. Borrnert, J. H. Warner, V. Hoffman, J. H. Lin, G. Cuniberti and B. Buchner, *ACS Nano*, 2010, **4**, 4206–4210.
67 J. Gong, J. Liu, X. Chen, Z. Jiang, X. Wen, E. Mijowska and T. Tang, *J. Mater. Chem. A*, 2014, **3**, 341–351.
68 M. A. Fanton, J. A. Robinson, C. Puls, Y. Liu, M. J. Hollander, B. E. Weiland, M. LaBella, K. Trumbull, R. Kasarda, C. Howsare and J. Stitt, *ACS Nano*, 2011, **5**, 8062–8069.
69 H. J. Song, M. Son, C. Park, H. Lim, M. P. Levendorf, A. W. Tsen, J. Park and H. C. Choi, *Nanoscale*, 2012, **4**, 3050–3054.
70 J. Lim, H. Yeo, M. Goh, B. C. Ku, S. G. Kim, H. S. Lee, B. Park and N. H. You, *Chem. Mater.*, 2015, **27**, 2040–2047.
71 G. Kalita, M. Matsushima, H. Uchida, K. Wakita and M. Umeno, *J. Mater. Chem.*, 2010, **20**, 9713–9717.
72 F. El-Tantawy, *Eur. Polym. J.*, 2001, **37**, 565–574.
73 F. El-Tantawy, K. Kamada and H. Ohnabe, *Mater. Lett.*, 2002, **56**, 112–126.
74 J. Yan and Y. G. Jeong, *Appl. Phys. Lett.*, 2014, **105**, 051907.
75 J. Lim, M. C. Kim, M. Goh, H. Yeo, D. G. Shin, B. C. Ku and N. H. You, *Carbon Letters*, 2013, **14**, 251–254.